

# Coexistence of Localized and Itinerant Electrons in the Double-Perovskite $\text{Ba}_2\text{Fe}_{2/3}\text{Mo}_{4/3}\text{O}_6$

Carlos A. López,<sup>\*[a]</sup> Martín E. Saleta,<sup>[b]</sup> José C. Pedregosa,<sup>[a]</sup>  
Rodolfo D. Sánchez,<sup>[b]</sup> José A. Alonso,<sup>[c]</sup> and  
María T. Fernández-Díaz<sup>[d]</sup>

**Keywords:** Iron / Molybdenum / Mixed-valent compounds / Magnetic properties / Perovskite phases

A polycrystalline  $\text{Ba}_2\text{Fe}_{2/3}\text{Mo}_{4/3}\text{O}_6$  double-perovskite has been prepared by decomposition of citrate precursors and subsequent thermal treatment under a reducing atmosphere. The crystal structure has been studied by combined X-ray and neutron powder diffraction (XRPD and NPD). At room temperature, the structure is cubic ( $\text{Fm}\bar{3}m$ ) with lattice parameter  $a = 8.0710(1)$  Å. It is unchanged between 3 and 320 K. The crystallographic formula is  $\text{Ba}_2[\text{Fe}_{0.52(2)}\text{Mo}_{0.48(2)}]_{4a}[\text{Fe}_{0.14(2)}\text{Mo}_{0.86(2)}]_{4b}\text{O}_{5.9(2)}$ . NPD, electron spin res-

onance (ESR), and magnetization measurements show spontaneous magnetization below the Curie temperature ( $T_C$ ) = 310 K. The ESR behavior is associated with the presence of localized  $\text{Fe}^{3+}$  ions, whereas the transport properties (electrical conductivity and Seebeck effect) suggest the presence of highly correlated electrons in a metallic band with disorder, which can be associated with the  $\text{Mo t}_{2g}$  electrons. The coexistence of localized and itinerant electrons leads to non-negligible magnetoresistance properties.

## Introduction

The search for materials with improved magnetotransport properties has been a topic of interest during the last decades in the field of transition-metal oxides, stimulated by their potential technological applications.<sup>[1]</sup> In particular, owing to the observation of colossal magnetoresistance (CMR), manganese perovskites rapidly became promising materials.<sup>[2]</sup> A few years after the discovery of this effect, attention also became focused on some double-perovskite oxides. The revival of interest in this family was triggered by a report on  $\text{Sr}_2\text{FeMoO}_6$ ,<sup>[3]</sup> which demonstrated that in the electronic structure only minority spins are present at the Fermi level; this material was shown to exhibit intrinsic tunneling-type magnetoresistance (TMR) at room temperature.<sup>[3,4]</sup> In a simple picture,  $\text{FeO}_6$  and  $\text{MoO}_6$  octahedra alternate along the three directions of the crystal structure of  $\text{Sr}_2\text{FeMoO}_6$ ; the system can be described as an ordered arrangement of parallel  $\text{Fe}^{3+}$  ( $S = 5/2$ ) magnetic moments antiferromagnetically coupled with  $\text{Mo}^{5+}$  ( $S = 1/2$ ) spins.

The magnetic and electron-transport properties in the  $\text{A}_2\text{FeMoO}_6$  (for  $\text{A} = \text{Ca}, \text{Sr}, \text{or Ba}$ ) system are strongly related to the degree of the Fe/Mo site ordering and the oxidation state of Fe and Mo.<sup>[5,6]</sup> In view of this, a number of experimental studies were directed to change this degree of ordering of Fe/Mo cations and their oxidation state. These experimental studies included: doping at the A site,<sup>[7–9]</sup> doping at Fe or Mo sites,<sup>[10–12]</sup> and changing the Fe/Mo ratio.<sup>[13–16]</sup> It is possible to shift from the oxidized form ( $\text{Fe}^{3+}\text{--Mo}^{6+}$ ) to the reduced form ( $\text{Fe}^{2+}\text{--Mo}^{5+}$ ) when the Fe/Mo ratio takes the limit values of 2 and 0.5, respectively, in  $\text{A}_2\text{Fe}_{1-x}\text{Mo}_{1+x}\text{O}_6$  stoichiometries. If  $\text{Fe}/\text{Mo} = 1$ , the standard  $\text{A}_2\text{FeMoO}_6$  formula contains pairs of  $\text{Fe}^{2+}\text{--Mo}^{6+}$  ions in equilibrium with  $\text{Fe}^{3+}\text{--Mo}^{5+}$  couples. When  $\text{Fe}/\text{Mo} = 2$ , the stoichiometry would be  $\text{A}_2\text{Fe}_{4/3}\text{Mo}_{2/3}\text{O}_6$  (equivalent to  $\text{A}_3\text{Fe}_2\text{MoO}_9$ ) in which all Fe and Mo ions are in an  $\text{Fe}^{3+}$  ( $t_{2g}^3e_g^2$ ) and  $\text{Mo}^{6+}$  ( $t_{2g}^0$ ) state, respectively.<sup>[17–19]</sup> Finally, if  $\text{Fe}/\text{Mo} = 0.5$ , the formula is  $\text{A}_2\text{Fe}_{2/3}\text{Mo}_{4/3}\text{O}_6$  (equivalent to  $\text{A}_3\text{Fe}_2\text{MoO}_9$ ) with Fe and Mo ions in the states  $\text{Fe}^{2+}$  and  $\text{Mo}^{5+}$ . Also, all the intermediate situations are possible, including those for which  $0.5 < \text{Fe}/\text{Mo} < 2$ . Whereas the cases with  $\text{Fe}/\text{Mo} = 1$  and 2 are well known,<sup>[13–16]</sup> the perovskites for  $\text{Fe}/\text{Mo} = 0.5$  (all Fe and Mo are as  $\text{Fe}^{2+}$  and  $\text{Mo}^{5+}$  reduced forms) have not been reported, and therefore their structure and physicochemical behaviors are unknown. Interesting magnetic and electric properties can be predicted in a system in which  $\text{Mo}^{5+}$  ( $t_{2g}^1$ ) with one itinerant electron and  $\text{Fe}^{2+}$  ( $t_{2g}^4e_g^2$ ) cations are stabilized. Furthermore, the fact that the end member perovskites  $\text{SrMoO}_3$  and  $\text{BaMoO}_3$  (both with  $\text{Fe}/\text{Mo} = 0$ ) exhibit metallic behavior with the highest conductivities ever observed

[a] INTEQUI – Área de Química General e Inorgánica “Dr. G. F. Puelles”, Facultad de Química, Bioquímica y Farmacia, Universidad Nacional de San Luis, Chacabuco y Pedernera, 5700 San Luis, Argentina  
E-mail: calopez@unsl.edu.ar  
<http://www.sanluis-conicet.gob.ar/intequi/>

[b] Centro Atómico Bariloche, Comisión Nacional de Energía Atómica y Instituto Balseiro, Universidad Nacional de Cuyo, 8400 S. C. de Bariloche, Río Negro, Argentina

[c] Instituto de Ciencia de Materiales de Madrid, CSIC, Cantoblanco, 28049 Madrid, Spain

[d] Institut Laue-Langevin, B.P. 156, 38042 Grenoble Cedex 9, France

in transition-metal oxides is appealing. In these materials the electrons of  $\text{Mo}^{4+}$  ( $t_{2g}^2$ ), are completely delocalized. Table 1 summarizes the intermediate and end situations of Fe/Mo ratio and the possible oxidation states.

Table 1.  $\text{A}_2\text{Fe}_{1-x}\text{Mo}_{1+x}\text{O}_6$  double-perovskites with different Fe/Mo ratios.

Fe/Mo ratio	$\text{A}_2\text{Fe}_{1-x}\text{Mo}_{1+x}\text{O}_6$	Oxidation states <sup>[a]</sup>
2	$\text{A}_2\text{Fe}_{4/3}\text{Mo}_{2/3}\text{O}_6$	$\text{Fe}^{3+}/\text{Mo}^{6+}$
1	$\text{A}_2\text{FeMoO}_6$	$\text{Fe}^{2+}/\text{Mo}^{6+} - \text{Fe}^{3+}/\text{Mo}^{5+}$
0.5	$\text{A}_2\text{Fe}_{2/3}\text{Mo}_{4/3}\text{O}_6$	$\text{Fe}^{2+}/\text{Mo}^{5+}$
0	$\text{AMoO}_3$	$\text{Mo}^{4+}$

[a] Expected oxidation states from the chemical point of view.

In the present work, we describe the synthesis of  $\text{Ba}_2\text{Fe}_{2/3}\text{Mo}_{4/3}\text{O}_6$  double-perovskite (Fe/Mo = 0.5) obtained by soft-chemistry procedures followed by thermal treatments under reducing conditions ( $\text{H}_2/\text{N}_2$ ). A well-crystallized sample was studied by X-ray and neutron powder diffraction, and its crystal structure was refined by the Rietveld method. To obtain a better understanding of this new system, we performed magnetic, electron-transport, magneto-transport, and thermoelectric measurements. The predominant  $\text{Fe}^{3+}$  oxidation state was confirmed by electron spin resonance (ESR).

## Results and Discussion

### Crystallographic Structure

The structural refinement was performed with combined X-ray powder diffraction (XRPD) and neutron powder diffraction (NPD) data at room temperature. The good agreement between the observed and calculated XRPD and NPD patterns after the refinement is shown in Figure 1a and b. The present sample was successfully refined as cubic in the space group  $Fm\bar{3}m$  based upon the model of the  $\text{Ba}_2\text{FeMoO}_6$  double-perovskite.<sup>[8–13]</sup>

In this space group (no. 225), the unit-cell parameter is related to  $a_0$  (ideal cubic perovskite,  $a_0 \approx 3.9 \text{ \AA}$ ) as  $a = 2a_0$ . Ba atoms were located at the  $8c$  ( $1/4, 1/4, 1/4$ ) positions, Fe/Mo at  $4a$  (0,0,0) and at  $4b$  ( $1/2, 1/2, 1/2$ ) sites, and oxygen atoms at the  $24e$  ( $x, 0, 0$ ) positions. For the  $Fm\bar{3}m$  space group there are two possible sites for B-type cations, namely,  $4a$  and  $4b$ . Minor amounts of  $\text{BaMoO}_4$  and elemental iron were detected as impurities and included in the refinement with their respective crystal structures defined in the space groups  $I4_1/a$  and  $Im\bar{3}m$ .<sup>[20,21]</sup> From the scale factor of the main and secondary phases we estimated the following impurity levels as: 1.0(4) and 0.6(4) wt.-% of  $\text{BaMoO}_4$  and  $\text{Fe}^0$ , respectively. Additionally, as this phase is magnetic at room temperature, we included a model for the magnetic structure, as described below.

Double-perovskites with stoichiometry  $\text{A}_2\text{B}'_{1-x}\text{B}''_{1+x}\text{O}_6$ , in which  $\text{B}'/\text{B}'' \neq 1$ , exhibit an intrinsic octahedral disorder, since some  $\text{B}'$  ions occupy  $\text{B}''$  sites and vice versa. In the present case with Fe/Mo = 0.5, the formula is  $\text{Ba}_2\text{Fe}_{2/3}\text{Mo}_{4/3}\text{O}_6$ , and Fe and Mo ions nominally exhibit

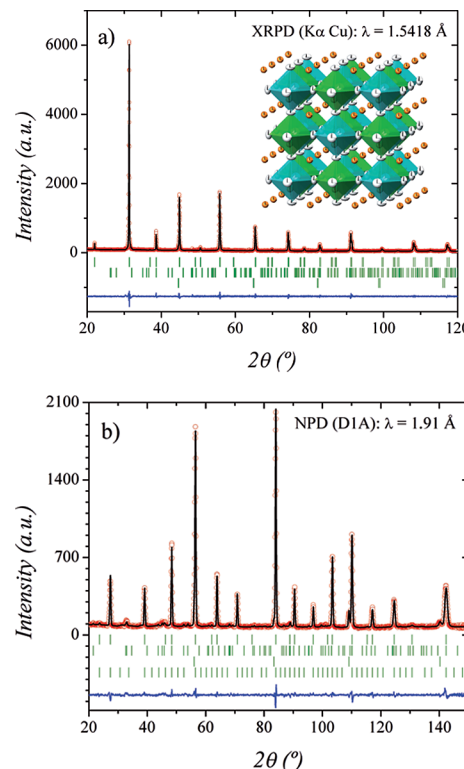


Figure 1. Observed (circles), calculated (full line), and difference (bottom) Rietveld profiles at room temperature for  $\text{Ba}_2\text{Fe}_{2/3}\text{Mo}_{4/3}\text{O}_6$  after a combined XRPD-NPD refinement. The second and third series of tick marks correspond to the Bragg reflections for the  $\text{BaMoO}_4$  and Fe impurity phases. (a) XRPD. Inset: schematic view of crystallographic structure showing  $\text{MoO}_6$  and  $\text{FeO}_6$  octahedra. (b) NPD. The fourth series of tick marks in NPD correspond to the Bragg reflections for the magnetic structure.

the states  $\text{Fe}^{2+}/\text{Mo}^{5+}$  or alternatively  $\text{Fe}^{3+}/\text{Mo}^{4.5+}$ . The degree of Fe/Mo disordering was experimentally refined, as well as the occupancy of oxygen positions. The final refined stoichiometry is  $\text{Ba}_2[\text{Fe}_{0.52(2)}\text{Mo}_{0.48(2)}]_{4a}[\text{Fe}_{0.14(2)}\text{Mo}_{0.86(2)}]_{4b}\text{O}_{5.9(2)}$ . The most important structural parameters of the crystallographic structure and the discrepancy factors after the refinements are listed in Table 1. Within the experimental error, the Fe/Mo ratio is 0.5, and the oxygen content can be considered stoichiometric. The fact that some Fe partially occupies the  $4b$  sites indicates the presence of some structural disordering beyond the intrinsic disorder given for this stoichiometry. If we call  $a$  the amount of Fe at  $4b$  sites, we can define the degree of order (DO) as  $\text{DO} = 1 - 3a$ .<sup>[18]</sup> For maximum order  $\text{DO} = 1$ , and for random distribution  $\text{DO} = 0$ . In the present case we observed  $\text{DO} = 0.58$ .

The thermal evolution of the crystallographic structure was investigated from NPD data sequentially collected from 3 to 320 K. The cubic model (space group  $Fm\bar{3}m$ ) was successfully considered in the whole temperature range. The average thermal expansion coefficient from 150 to 320 K is  $11.3 \times 10^{-6} \text{ K}^{-1}$ . The thermal evolution of the  $a$  unit-cell parameter and distances  $\langle \text{Fe/Mo-O} \rangle$  are shown in Figure 2; they display a weak temperature dependence. Fig-

Figure 2 also includes the expected distances for different oxidation states for Fe and Mo.

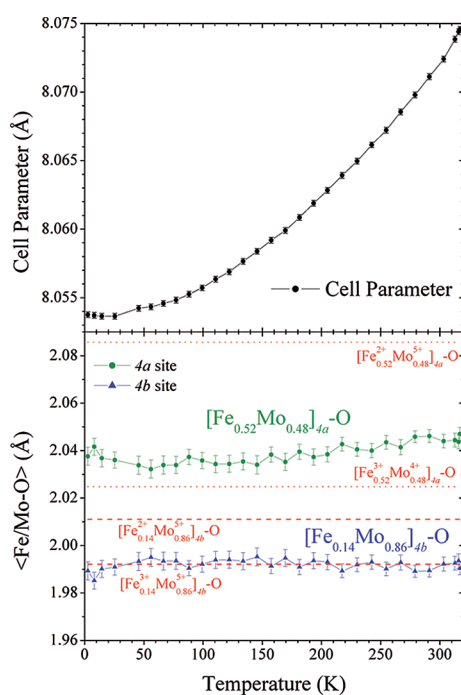


Figure 2. Top panel:  $a$  unit-cell parameters as a function of temperature. Bottom panel: octahedral size  $\langle \text{Fe}/\text{Mo}-\text{O} \rangle$  as a function of temperature for both crystallographic B sites. Dotted and dashed lines indicate the expected distances for different oxidation states for Fe and Mo.

Considering the stoichiometry  $\text{Ba}_2\text{Fe}_{2/3}\text{Mo}_{4/3}\text{O}_6$ , and from the chemical point of view, we expected that the oxidation states would be between  $\text{Ba}_2\text{Fe}^{2+}_{2/3}\text{Mo}^{5+}_{4/3}\text{O}_6$  and  $\text{Ba}_3\text{Fe}^{3+}_{2/3}\text{Mo}^{4.5+}_{4/3}\text{O}_6$ . The structural analysis might help to ascertain the true configuration. As shown in Table 1, the  $\langle \text{Fe}/\text{Mo}-\text{O} \rangle$  distances at room temperature are 2.045(1) and 1.990(1) Å for the 4a and 4b sites, respectively. The comparison with the expected distances for different possibilities for the oxidation states of Fe and Mo suggests that in the electronic configurations for the 4b site the distances are close to those expected to  $\text{Fe}^{3+}\text{Mo}^{5+}$ , whereas for the 4a site they are closer to  $\text{Fe}^{3+}\text{Mo}^{4+}$  than to  $\text{Fe}^{2+}\text{Mo}^{5+}$ .

### Thermogravimetric Analysis

Figure 3 illustrates the TGA curves in air (oxidation process) of  $\text{Ba}_2\text{Fe}_{2/3}\text{Mo}_{4/3}\text{O}_6$ . The samples are stable in an air flow up to 575 K; above this temperature, an oxidation process starts. The final products were identified by XRPD allowing for the reaction according to [Equation (1)].



The experimental weight gain for these reactions (2.8%) is in agreement with the theoretical ones (2.9%). These facts indicate that, within the experimental error, Fe and Mo ions are as  $\text{Ba}_2\text{Fe}^{2+}_{2/3}\text{Mo}^{5+}_{4/3}\text{O}_6$  or the equivalent isoelectronic state  $\text{Ba}_3\text{Fe}^{3+}_{2/3}\text{Mo}^{4.5+}_{4/3}\text{O}_6$ , which are indiscernible. There-

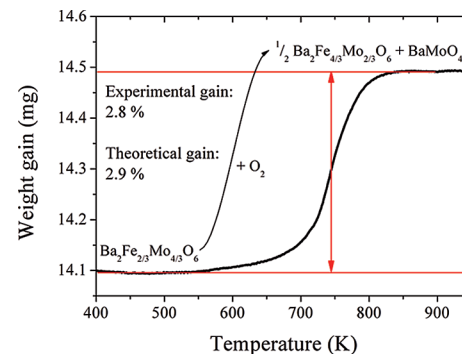


Figure 3. TGA curves of  $\text{Ba}_2\text{Fe}_{2/3}\text{Mo}_{4/3}\text{O}_6$  sample (oxidation process) obtained in air flow at  $5 \text{ K min}^{-1}$ .

fore, the sample presents an  $\text{Fe}(3d^{6-\delta})-\text{Mo}(4d^{1+\delta/2})$  configuration with  $0 < \delta < 1$ . From the structural information described above, including the thermal evolution of the distances (Figure 2), we can assume that the  $\delta$  value is close to 1.

### Magnetic Structure

As previously mentioned, the NPD pattern at room temperature shows a magnetic contribution to the scattering on allowed Bragg positions ( $k = 0$ ), mainly on the (111) reflection, which suggests a ferro- or ferrimagnetic long-range ordering. The magnetic contribution is enhanced upon cooling, as is clearly shown in the thermal evolution of the NPD patterns (Figure 4). We have fit the magnetic contributions to the neutron scattering by modeling a ferrimagnetic structure that consists of a collinear arrangement of two sets of spins with opposite directions at the 4a and 4b sites, which corresponds to the B positions of the perovskite structure, with the same unit-cell parameters as the crystallographic  $\text{Ba}_2\text{Fe}_{2/3}\text{Mo}_{4/3}\text{O}_6$  phase. The magnetic moments of both sets have been constrained to the relationship

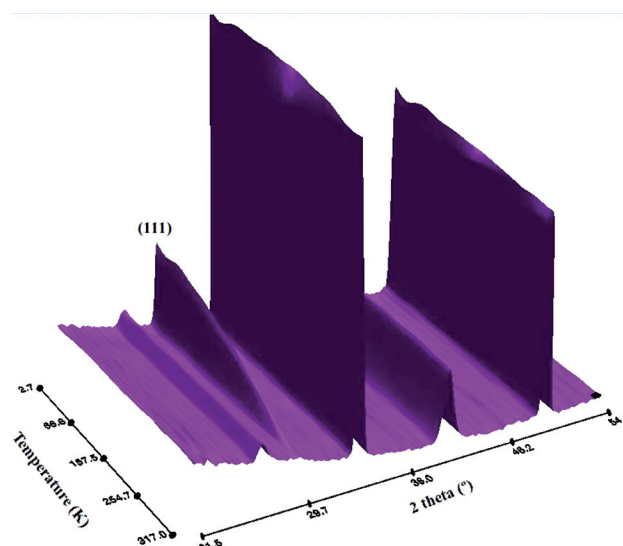


Figure 4. Thermal evolution of NPD patterns, with  $\lambda = 2.492 \text{ \AA}$ , collected sequentially.

that exists between the Fe contents of  $4a$  versus  $4b$  sites ( $0.52/0.14$ ). After refinement, the ordered magnetic moments for  $4a$  and  $4b$  sites are  $2.6$  and  $0.7 \mu_B$ , respectively. These values can be obtained by multiplying the magnetic moment of  $\text{Fe}^{3+}$  ( $3d^5$ ) of  $5 \mu_B$  for its occupation of each site. The good agreement between observed and calculated NPD patterns at  $3\text{ K}$  is shown in Figure 5a. The thermal variation of the magnitude of the ordered  $4a$  and  $4b$  magnetic moments is displayed in Figure 5b.

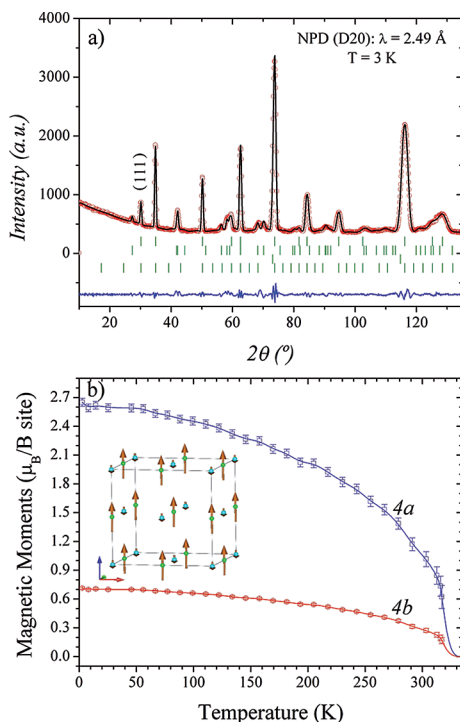


Figure 5. (a) Rietveld plots after the refinement of the crystal structure and magnetic structure from NPD data at  $T = 3\text{ K}$ . The line at the bottom is the difference between calculated and experimental patterns. The four sets of Bragg reflections correspond to the main crystallographic phase,  $\text{BaMoO}_4$ , metal Fe, and the magnetic phase, respectively. (b) Thermal dependence of the ordered magnetic moments refined from NPD data. The inset shows a schematic view of the magnetic structure.

## Magnetic Properties

The magnetization ( $M$ ) versus temperature curve is displayed in Figure 6. The sample has a spontaneous increment of the magnetization below  $310\text{ K}$ . The Curie temperature ( $T_C$ ) was determined as the minimum value in the  $dM/dT$  versus  $T$  curve (see Figure 6). This temperature is in excellent agreement with that determined from temperature-dependent NPD data, which also shows that the long-range magnetic ordering is established close to  $310\text{ K}$ .

Above  $T_C$ , the temperature range is too narrow to perform a Curie–Weiss fit. In similar phases with high  $T_C$  values it was also difficult to obtain information on the paramagnetic region owing to the existence of antisite defects or the presence of spurious ferromagnetic impurities, which mask the paramagnetic behavior.<sup>[22,23]</sup>

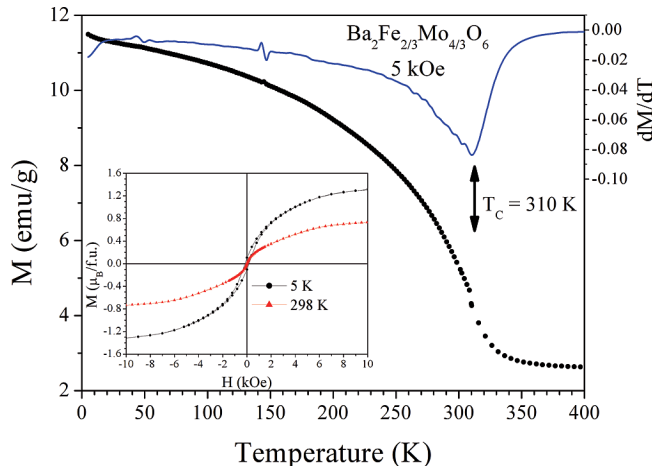


Figure 6. Magnetization (left axis) and first derivative of the magnetization (right axis) as a function of temperature at  $5\text{ kOe}$ . The inset shows the magnetizations versus field loops at  $5\text{ K}$  and  $298\text{ K}$ .

The magnetization versus magnetic field curve at  $5\text{ K}$  and room temperature is plotted in the inset of Figure 6. At both temperatures, the maximum magnetization values measured for the higher applied field of  $H = 10\text{ kOe}$  reach ca.  $0.7$  and  $1.3 \mu_B$  per formula unit (f.u.) at  $298$  and  $5\text{ K}$ , respectively. In a completely localized moment picture, the global ferromagnetism is the result of the microscopically unbalanced occupancy of  $4a$  and  $4b$  sites by Fe and Mo ions. Assuming that the coupling between neighbors through common oxygen atoms (either  $\text{Fe}–\text{O}–\text{Fe}$ , or  $\text{Fe}–\text{O}–\text{Mo}$ , or  $\text{Mo}–\text{O}–\text{Mo}$ ) is always antiferromagnetic (AFM), the coherence across the crystal is perfectly maintained, and the saturation magnetization is the result of the different occupation between the crystallographic  $4a$  and  $4b$  sites. For this model, considering  $\text{Fe}^{3+}$  ( $S = 5/2$ ) and equimolar amounts of  $\text{Mo}^{4+}$  ( $S = 1$ ) and  $\text{Mo}^{5+}$  ( $S = 1/2$ ), we would obtain a saturation magnetization of  $1.33 \mu_B$  per f.u., in perfect agreement with the observed magnetization value at  $5\text{ K}$  of  $1.3 \mu_B$  per f.u. However, when observed in detail, the  $M$ – $H$  loops have an elongated “S” shape with a small coercive field (approximately  $H_c = 160$ – $180$  Oe at low temperatures). Both sides of the loop, upon increasing and decreasing  $H$ , can be described by a Langevin function [ $M/M_s = \coth(x) - 1/x$ , in which  $x = \mu(H \pm H_c)/kT$  and  $M_s$  is the saturation magnetization]. This behavior can be associated with the rotation of the net magnetization of small regions (“FM clusters”), which can interact between them through the itinerant Mo ( $t_{2g}$ ) electrons. It is an alternative picture in which the uncompensated localized  $\text{Fe}^{3+}$  ions produce a net magnetization in the material, which is reinforced by the presence of itinerant  $t_{2g}$  electrons.

The ESR spectra were collected in the temperature range  $100\text{ K} < T < 350\text{ K}$ ; some selected spectra are shown in Figure 7. The obtained ESR line shape is Lorentzian, as expected for ceramic samples reduced to a fine powder. The spectra for  $T < T_C$  are shown in Figure 7a. The magnetic resonance field is shifted to the paramagnetic value, and the line is narrowed with increasing  $T$ . Yet the spectra for  $T >$

$T_C$  (shown in Figure 7b) present a constant value of the resonant magnetic field ( $H_R$ ) that corresponds to  $g = 2.05$ . We discard the possibility of assigning the observed resonance to localized  $\text{Fe}^{2+}$ , because its ground state in an octahedral environment is a triplet with an expected  $g$  factor of about 3.4, which is far from our measured value. However, as  $\text{Fe}^{2+}$  presents an usually short relaxation time, it would render their ESR line undetectable, as in the case of  $\text{FeO}$ . This obtained value is close with a spin-only ground state that principally corresponds to the localized  $3d^5 \text{Fe}^{3+}$  (1.997  $\leq g \leq 2.003$ )<sup>[24]</sup> and it is similar to that reported for  $\text{Sr}_2\text{FeMoO}_6$ <sup>[22,23]</sup> perovskite, in which the itinerant electrons of Mo ions contribute to shift the  $\text{Fe}^{3+}$   $g$  value a little.

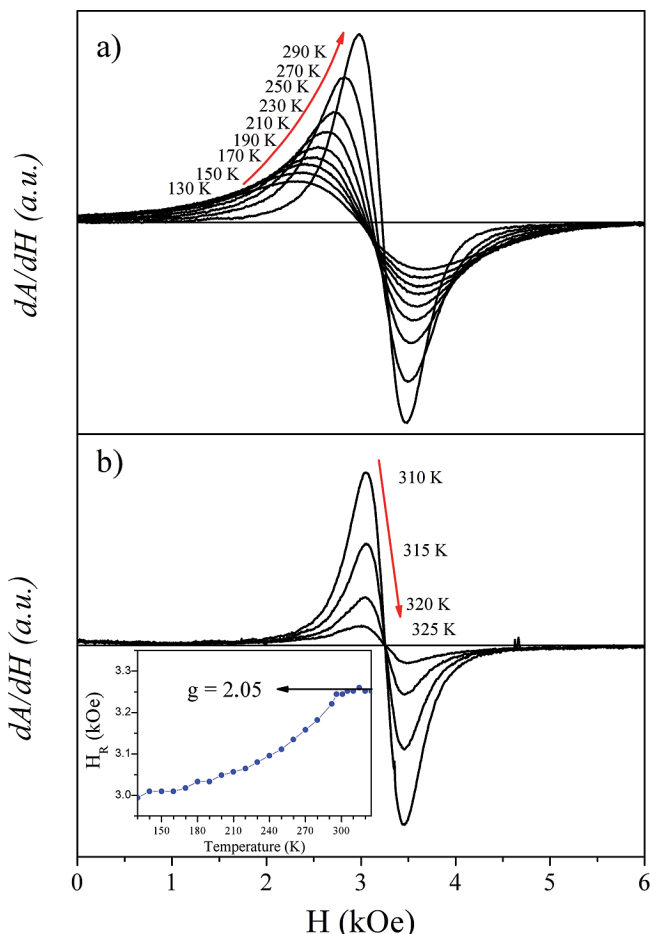


Figure 7. (a) ESR spectra (absorption derivatives) at several temperatures: (a) below  $T_C$  and (b) in the paramagnetic region. The inset shows the resonance field ( $H_R$ ) versus temperature.

The temperature dependence of  $H_R$  is shown in the inset of Figure 7, which also shows the magnetic-field resonance expected for paramagnetic  $\text{Fe}^{3+}$  ions. Below  $T_C$ ,  $H_R$  values diminish as  $T$  decreases owing to the internal magnetic field that comes from the magnetic order inside the sample, thus demonstrating that the  $\text{Fe}^{3+}$  ions are part of the magnetic lattice. This result is also supported by NPD experiments, in which the presence of  $\text{Fe}^{3+}$  is evidenced by the average Fe/Mo–O distances.

The experimental peak-to-peak line width ( $\Delta H_{PP}$ ) and the line intensity ( $I_{ESR}$ ) for the crystalline powder of  $\text{Ba}_2\text{Fe}_{2/3}\text{Mo}_{4/3}\text{O}_6$  as a function of temperature are shown in Figure 8. The  $\Delta H_{PP}$  shows a minimum of approximately 380 Oe at  $T_{min} \approx T_C$ . Below this temperature  $\Delta H_{PP}(T)$  increases with decreasing  $T$  to reach values of 1500 Oe at 130 K. Above  $T_{min}$ ,  $\Delta H_{PP}$  increases with  $T$  to reach 650 Oe at 350 K. The  $I_{ESR}$  shows the same behavior as the macroscopic magnetization of the compound (Figures 5b and 6). All the ESR parameters present the expected behavior of a ferromagnetic material.

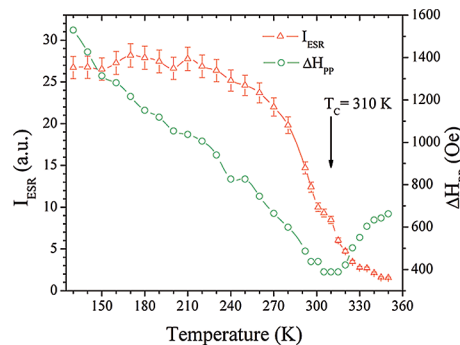


Figure 8. ESR intensity ( $I_{ESR}$ ) (left axis) and peak-to-peak linewidth ( $\Delta H_{PP}$ ) (right axis) as a function of temperature.

The Curie temperature is also observed in the ESR experiments. The ESR lines reach a constant value of the resonant magnetic field at 310 K, as observed in Figure 7b. The  $\Delta H_{PP}$  presents a minimum value close to  $T_C$  in the same way as other similar compounds.<sup>[22,23]</sup> One of the common problems in the ESR results of samples in which one of the cations is  $\text{Fe}^{3+}$  is the observation of spurious magnetic impurities as ferromagnetic iron oxides. In general, their strong ESR signal masks the response of the material in focus. However, in this case, the ESR intensity as a function of temperature (Figure 7) presents the same spontaneous magnetization and  $T_C$  as that observed by other two techniques: the magnetic moment per site (NPD), which is represented in Figure 5b, and by the magnetization curves as a function of temperature plotted in Figure 6. This corroborates that the ESR signal is the response of the magnetic ions contained by the double-perovskite under study and is not from spurious magnetic phases.

## Electron-Transport Properties

The electrical resistivity of the  $\text{Ba}_2\text{Fe}_{2/3}\text{Mo}_{4/3}\text{O}_6$  perovskite was performed from 300 to 80 K. As shown in Figure 9, at room temperature the resistivity is  $191 \Omega\text{cm}^{-1}$ . The resistivity increases quickly from 300 to 280 K, and then the resistivity increases smoothly up to 80 K. The negative slope value of the resistivity versus temperature data could be associated with a semiconductor response of the material, but the absolute  $\rho$  values are relatively low ( $\rho < 10^2 \Omega\text{cm}^{-1}$ ), which might indicate that the Fermi level of the material, close to the mobility border of the electrons, occupies localized states in a metallic band owing to the

presence of disorder. The theory predicts, for highly correlated electrons in metals with disorder, that the thermal behavior of the electrical conductivity must follow  $\sigma(T) = \sigma_0 + A \cdot T^{1/2}$ .<sup>[25]</sup> This thermal and linear behavior of the conductivity with the square root of the temperature can be viewed in the inset of Figure 9, thereby confirming that this double-perovskite is metallic with highly correlated electrons under a disorder potential. It is noteworthy that this effect is observed in this double-perovskite at immediately below  $T_C$ , unlike  $V_2O_3$  and doped semiconductors Si:P, in which this effect is observable at low temperature, or also unlike the clear metallic state observed in the perfectly ordered  $Sr_2FeMoO_6$  double-perovskite.<sup>[25]</sup>

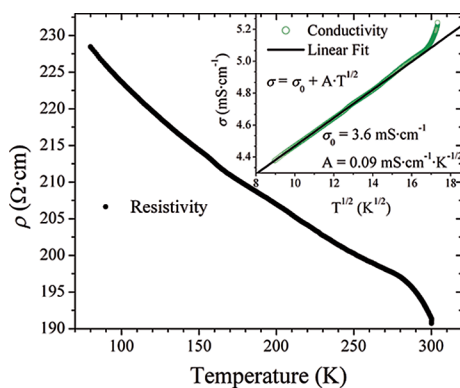


Figure 9. Electrical resistivity as a function of temperature. The inset shows the linear behavior of  $\sigma = \sigma_0 + T^{1/2}$ .

Figure 10 shows the thermal variation (cooling and warming) of the Seebeck coefficient ( $S$ );  $S$  is a zero-current transport coefficient, and it was measured using the standard temperature differential technique. It is a very useful proof to discern between semiconductor and metallic behavior. The  $S$  values are negative and show a linear behavior in the measured temperature range. This behavior has also been observed in double-perovskite systems such as  $A_2FeMoO_6$ ,<sup>[26–28]</sup> and it is remarkably similar to that found in the metallic phase of the high-temperature superconducting cuprates<sup>[29]</sup> and manganites.<sup>[30]</sup> In general, the diffusion term of the thermoelectric power coming from an electron gas is described by the Mott formula [ $S_d = (\pi^2 k_B^2 T / 3e)(\partial \ln \sigma / \partial e)\varepsilon_F$ ].<sup>[31]</sup> The  $(\partial \ln \sigma / \partial e)\varepsilon_F$  is a generalization, which is associated with the energy at the Fermi surface ( $\varepsilon_F$ ). The Mott formula is linear with temperature;  $\pi$ ,  $k_B$ , and  $e$  are constants and the last term can be reduced, according to the model, to a constant value, too. The slope of the  $S$  versus  $T$  data is  $-0.024 \mu V K^{-2}$ . In the limit when  $T \rightarrow 0$ , also  $S \rightarrow 0$ . An extra contribution should be present at the Seebeck coefficient, which can be the phonon drag contribution. It has a maximum value around a fraction of the Debye temperature ( $\Theta_D/3$ ), and the contribution decreases as  $1/T$ . We use the model of Trodahl<sup>[29]</sup> to interpret the  $S$  coefficients in terms of a phonon drag component (dashed line) and a diffusion term (dotted line). This behavior has also been observed in double-perovskite systems such as  $A_2FeMoO_6$ .<sup>[26–28]</sup>

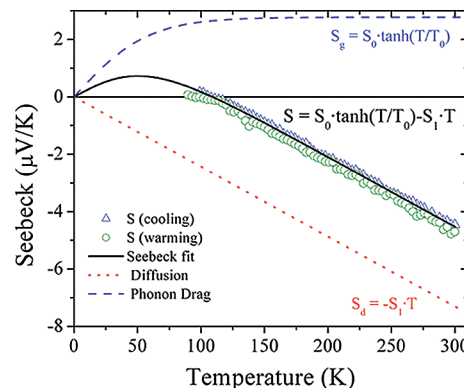


Figure 10. Seebeck coefficient as a function of temperature. The dashed line represents the temperature dependence of a contribution to the phonon drag thermopower, labeled  $S_g$ , from a typical phonon in the acoustic branch. The diagram also shows a negative diffusion contribution  $S_d$  (dotted line) and illustrates how the observed thermopower results from a sum of the two contributions (solid line).

The electrical resistance was also measured as a function of magnetic field at room temperature and at 90 K (see Figure 11a). The measurement at room temperature showed a negligible effect with a magnetic field of 3 kOe. However, at 90 K a magnetoresistive effect was clearly observed. Figure 11 shows the magnetoresistance (MR) defined as  $\Delta R/R$  (%) =  $100 \times [\rho(H) - \rho(0)]/\rho(0)$  as a function of  $H/T$ . A negative magnetoresistance is observed; it reaches a maximum MR of  $-1.5\%$  at 3 kOe. The  $\Delta R/R$  versus  $H/T$  plot also showed an interesting hysteresis, the maximum value of which can be associated with the coercive field of the sample measured in the hysteresis loop.

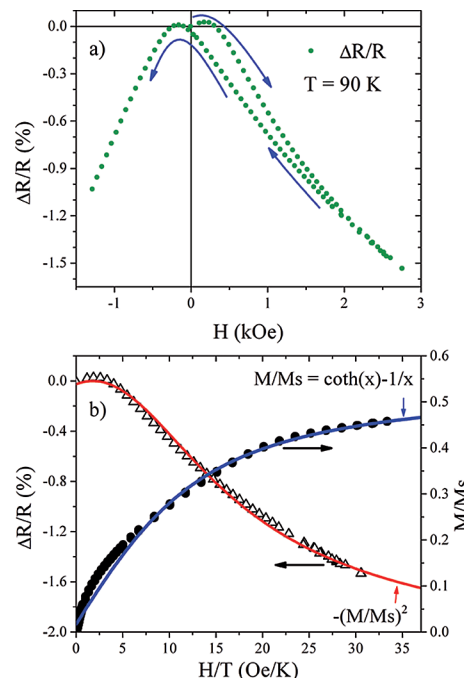


Figure 11. (a) Magnetoresistance ( $\Delta R/R$ ) as a function of magnetic field at 90 K. (b)  $\Delta R/R$  (left axis) and  $M/M_s$  (right axis) as a function of  $H/T$ .

However, the electrical resistivity also presents an anomalous behavior close to room temperature. The coexistence of important electronic conductivity and FM cluster interactions below  $T_C$  accounts for the magnetotransport properties, as observed in other half-metallic double-perovskites. In  $\text{Sr}_2\text{FeMoO}_6$  the extra itinerant Mo electrons occupy down-spin bands and they are shared among Fe and Mo atoms. In the  $\text{Ba}_2\text{Fe}_{2/3}\text{Mo}_{4/3}\text{O}_6$  system there are itinerant (associated with Mo) and localized (associated with Fe) electrons, as shown from NPD data, whereby the localized Fe spins contribute to the magnetic scattering and to the EPR signal, and, on the other hand, the transport and Seebeck measurements, which show a clear metallicity and itinerancy of some electrons. But the parallelism with  $\text{Sr}_2\text{FeMoO}_6$  is not complete, since significant differences can be noted from the results of the present study. One of them is the magnetic behavior with  $H$ , in which the presence of regions with FM clusters can be described with a Langevin function.

The MR properties would be a result of the spin-dependent scattering of the charge carriers through the magnetically ordered regions; this scattering is reduced when an external magnetic field is applied, thus aligning the orientation of the isolated clusters. The maximum value of MR ( $-1.5\%$ ) was measured at 90 K (see Figure 11a). The observed increase in MR as the magnetic field increased is similar to that exhibited in other double-perovskites, namely,  $\text{Sr}_2\text{FeMoO}_6$ , in which the main component of MR is attributable to grain boundary tunneling effects that take place at temperatures well below  $T_C$ ; however, in our case the magnetoresistive effect is lower than in  $\text{Sr}_2\text{FeMoO}_6$  or  $\text{Ba}_2\text{FeMoO}_6$ .<sup>[32,33]</sup> In general, the MR is proportional to the square of the magnetization, and in this case the experimental MR versus  $H/T$  curve can be successfully reproduced by considering the square of the Langevin equation and the hysteresis process of 150 Oe approximately. This can be seen in Figure 11b, in which the  $\Delta R/R$  versus  $H/T$  plot is correctly described with this model.

To summarize,  $\text{Ba}_2\text{Fe}_{2/3}\text{Mo}_{4/3}\text{O}_6$  is a partially disordered perovskite that presents FM-cluster or small-FM-region behavior below 310 K and the coexistence of localized  $\text{Fe}^{3+}$  with itinerant electrons from the Mo ions. As in  $\text{Sr}_2\text{FeMoO}_6$ , the electron itinerancy arises from down-spin Mo  $4d^{1+\delta/2}$  electrons of  $t_{2g}$  character. The decrease in the Fe content, realized in the perovskite end-member  $\text{SrMoO}_3$ , leads to a metallic state with a total electron delocalization. In the present case, we are dealing with intermediate Fe content in which Fe electrons occupy localized states, whereas majority Mo electrons are itinerant and account for the transport properties. The high magnetic-ordering temperature is therefore the result of direct antiferromagnetic superexchange Fe–O–Fe interactions combined with the presence of itinerant Mo  $t_{2g}$  electrons. This magnetic state is promoted by a structural disorder ( $\text{DO} = 0.58$ ), which promotes the occurrence of Fe atoms with different environments, from Fe–O–(Fe<sub>6</sub>) to Fe–O–(Mo<sub>6</sub>), and all the intermediate situations.<sup>[18]</sup> The net magnetization of this compound can be described by a Langevin function. The

electric properties can be understood in the context of a disordered metal that presents negative magnetoresistance, which is dominated by the scattering between the itinerant electrons with the magnetic field alignment of the ferromagnetic region polarization.

## Conclusion

A new double-perovskite,  $\text{Ba}_2\text{Fe}_{2/3}\text{Mo}_{4/3}\text{O}_6$ , with Fe/Mo mixed-valence states and a configuration close to  $\text{Fe}^{3+}\text{--Mo}^{4.5+}$  has been obtained by citrate techniques followed by an annealing in an  $\text{H}_2/\text{N}_2$  flow at 800 °C. The crystal structure is cubic with space group  $Fm\bar{3}m$  in the temperature range 3–320 K; the average thermal expansion coefficient is  $11.3 \times 10^{-6} \text{ K}^{-1}$ . The crystallographic formula obtained at room temperature,  $\text{Ba}_2[\text{Fe}_{0.52(2)}\text{Mo}_{0.48(2)}]_{4a}[\text{Fe}_{0.14(2)}\text{--Mo}_{0.86(2)}]_{4b}\text{O}_{5.9(2)}$ , involves an important antisite disordering, which accounts for the observed magnetic properties. The magnetic ordering temperature is  $T_C = 310$  K, as shown from magnetization and NPD data. This high magnetic-ordering temperature is the result of direct antiferromagnetic superexchange Fe–O–Fe interactions combined with the presence of itinerant Mo  $t_{2g}$  electrons. The magnetic structure at 3 K has been successfully refined by modeling a ferrimagnetic-like arrangement of two sets of spins with opposite directions at the  $4a$  and  $4b$  sites that correspond to the B positions of the perovskite structure. The uncompensated magnetization of the crystallographic sites results in a net ferromagnetic component. The magnetization behavior can be described with a Langevin function.

The electric conductivity shows a square-root temperature dependence, which is characteristic of disordered metals and is observed in deficient vanadium oxide, doped semiconductors, and  $\text{La}_{1-x}\text{Sr}_x\text{CoO}_3$ . A magnetoresistance as high as  $-1.5\%$  for  $H = 3$  kOe is observed at 90 K. The Seebeck effect is the result of two contributions: one of them is the phonon drag component, and the second is characteristic of high conductivity samples with itinerant electrons in a conduction band.

## Experimental Section

The  $\text{Ba}_2\text{Fe}_{2/3}\text{Mo}_{4/3}\text{O}_6$  double-perovskite was prepared as a black polycrystalline powder from citrate precursors obtained by soft-chemistry procedures under a controlled atmosphere. Stoichiometric amounts of analytical-grade  $\text{Ba}(\text{NO}_3)_2$ ,  $\text{Fe}(\text{NO}_3)_3 \cdot 9\text{H}_2\text{O}$ , and  $(\text{NH}_4)_6\text{Mo}_7\text{O}_{24} \cdot 4\text{H}_2\text{O}$  were dissolved in citric acid. The polymerization of the citrate solution upon gentle heating led to organic resins that contained a random distribution of the cations involved at an atomic level. These resins were first dried at 180 °C, and then all the organic materials and nitrates were eliminated in a subsequent treatment at 600 °C in air for 12 h, thus giving rise to highly reactive precursor materials.

The conditions for the  $\text{Ba}_2\text{Fe}_{2/3}\text{Mo}_{4/3}\text{O}_6$  synthesis were established from several trials under different conditions of temperature and time, in  $\text{H}_2/\text{N}_2$  (5:95) atmosphere. The tested final temperatures were 700, 750, 800, 850, 900, and 950 °C. The optimal synthesis conditions were found after treatment under  $\text{H}_2/\text{N}_2$  (5:95) atmo-

sphere at 800 °C for 12 h. The rate of heating and cooling was 5 °C min<sup>-1</sup>. Thermal treatments longer than 12 h did not produce changes in the quality of the samples, thus suggesting that the equilibrium with the atmosphere is reached before this treatment time. In Table 2 we summarize the different temperatures tested and the phases obtained in each case. It is worth commenting that trials to obtain the same phase with Sr instead of Ba did not lead to single perovskite phases but a mixture of oxides. Different aliquots, in powder form, from a unique batch obtained from the synthesis were used for the measurements.

**Table 2.** Phases observed by XRPD (indicated with crosses) at different synthesis temperatures.

T [°C] (12 h)	Main phase $\text{Ba}_2\text{Fe}_{2/3}\text{Mo}_{4/3}\text{O}_6$	Spurious phases		
		$\text{BaMoO}_4$	$\text{Fe}^0$	$\text{BaMoO}_3$
700		x		
750		x		
800 <sup>[a]</sup>	x	x	x	
850	x	x	x	
900	x		x	x
950		x	x	

[a] Best synthesis conditions; sample selected for the study.

The initial identification and characterization of the samples as well as the crystallographic study were carried out from XRPD patterns collected at room temperature. The experimental XRPD patterns were obtained with a Rigaku D-MAX-IIIC diffractometer with Cu- $K_\alpha$  ( $\lambda = 1.5418 \text{ \AA}$ ) radiation. The data were collected over a range of 10–120° (2θ) with a step of 0.02°; the effective counting time was 5 s per step (Table 3).

For the structural refinements, NPD patterns were collected at room temperature with a D1A neutron diffractometer at  $\lambda = 1.910 \text{ \AA}$ . The thermal evolution of the crystallographic and magnetic structures was carried out from NPD patterns sequentially collected with a D20 diffractometer at a wavelength of 2.492 Å; both instruments (D1A and D20) belong to the Institute Laue Langevin (ILL), Grenoble, France. The patterns were refined by the Rietveld method<sup>[34]</sup> using the FULLPROF refinement program.<sup>[35]</sup> A pseudo-Voigt function was chosen to generate the line shape of the diffraction peaks. In the final runs, the following parameters were refined: scale factors for the main and impurity phases, background coefficients, zero-point error, unit-cell parameters, pseudo-Voigt-corrected asymmetry parameters, positional coordinates, anisotropic thermal factors, and antisite disorder of Fe/Mo and occupancy factors for oxygen atoms. The coherent scattering lengths for Ba, Fe, Mo, and O were 5.05, 9.45, 6.72, and 5.803 fm, respectively.

Thermogravimetric analysis was performed with a Shimadzu TG-50H thermal analyzer apparatus using flowing air at 50 mL min<sup>-1</sup> from 298 to 1273 K at a heating rate of 5 K min<sup>-1</sup>. About 18 mg of the sample was used in the experiment.

Magnetic susceptibility was measured with a commercial SQUID magnetometer on powdered samples in the temperature range of 5–330 K and in a commercial VSM magnetometer in the range of 298–400 K.

The electrical-transport properties were determined with homemade equipment. The experiments were carried out between 80 and 300 K. In the case of the electrical resistivity, it was measured by the conventional four-probe technique. To obtain the magnetotransport response, the electrical resistance was taken under magnetic fields up to 3 kOe, and the thermoelectric power was obtained from the slope of the voltage generated by a thermal variation using a temperature ramp of 3 K in temperature with respect to the fixed

**Table 3.** Crystallographic data for the  $\text{Ba}_2\text{Fe}_{2/3}\text{Mo}_{4/3}\text{O}_6$  phase. System: cubic; space group:  $Fm\bar{3}m$ .

Crystallographic data from combined XRPD and NPD ( $\lambda = 1.91 \text{ \AA}$ ) data at r.t.; $a = 8.0710(1) \text{ \AA}$ , $V = 525.76(1) \text{ \AA}^3$						
Atom	Wyckoff site	x/a	y/b	z/c	$B_{\text{iso}} [\text{\AA}^2]$	Occ
Ba	8c	0.25	0.25	0.25	0.29	1
Fe1	4a	0	0	0	0.25	0.52(2)
Mo1	4a	0	0	0	0.25	0.48(2)
Fe2	4b	0.5	0.5	0.5	0.16	0.14(2)
Mo2	4b	0.5	0.5	0.5	0.16	0.86(2)
O	24e	0.2534(7)	0	0	0.50	0.99(3)

(b) Main distances		AO <sub>12</sub> polyhedral	
[Fe/Mo]O <sub>6</sub> octahedral		Ba–O(×12)	2.854(4) Å
(Fe/Mo) <sub>4a</sub> –O(×6)	2.045(1) Å		
(Fe/Mo) <sub>4b</sub> –O(×6)	1.990(1) Å		

Crystallographic data from NPD ( $\lambda = 2.49 \text{ \AA}$ ) data at 3 K, $a = 8.0537(2) \text{ \AA}$ , $V = 522.38(2) \text{ \AA}^3$						
Atom	Wyckoff site	x/a	y/b	z/c	$B_{\text{iso}} [\text{\AA}^2]$	Occ
Ba	8c	0.25	0.25	0.25	0.70	1
Fe1	4a	0	0	0	0.74	0.52
Mo1	4a	0	0	0	0.74	0.48
Fe2	4b	0.5	0.5	0.5	0.40	0.14
Mo2	4b	0.5	0.5	0.5	0.40	0.86
O	24e	0.2466(8)	0	0	0.40	1

NPD: $R_p = 2.41\%$ , $R_{\text{wp}} = 3.29\%$ , $R_{\text{exp}} = 0.83\%$ , $\chi^2 = 15.0$ , $R_{\text{Bragg}} = 8.21\%$ .			
(b) Main distances			
[Fe/Mo]O <sub>6</sub> octahedral		AO <sub>12</sub> polyhedral	
(Fe/Mo) <sub>4a</sub> –O(×6)	2.038(4) Å	Ba–O(×12)	2.848(3) Å
(Fe/Mo) <sub>4b</sub> –O(×6)	1.989(4) Å		

temperature of one end of the sample. For these electron-transport experiments, polycrystalline powder was pressed in bar-shaped pellets and sintered at 800 °C for 6 h in an Ar flow. These sintering conditions were used to obtain a ceramic sample equivalent to the powdered samples in such a way that either the chemical composition or the physical properties are unaltered by the process.

The ESR experiments were performed at 9.5 GHz (X-band) with a Bruker ESP-300 spectrometer from 100 to 350 K. The powder sample was reground and diluted with KCl (approx. 1:5) to fill the whole length of the resonator to warrant a uniform microwave field.

## Acknowledgments

J. C. P. thanks Consejo Nacional de Investigaciones Científicas y Técnicas (CONICET) (project PIP 112-200801-01360), Secretaría de Ciencia y Tecnología de la Universidad Nacional de San Luis (SECyT-UNSL) (project PROICO 2-7707-22/Q823), and Agencia Nacional de Promoción Científica y Tecnológica (ANPCyT) (project PICT 6/25459). R. D. S. thanks Universidad Nacional de Cuyo (UNCuyo), CONICET, and ANPCyT (Argentina) under grants 06/C389, PIP-490, and PICT2007-0832/PICT2011-0752. J. C. P., R. D. S., C. A. L., and M. E. S. are members of CONICET. J. A. A.

acknowledges the financial support of the Spanish Ministry of Education on the project MAT2007-60536. We are grateful to ILL for making all facilities available.

- [1] J. L. Simonds, *Phys. Today* **1995**, *48*, 26.
- [2] M. B. Salamon, M. Jaime, *Rev. Mod. Phys.* **2001**, *73*, 583.
- [3] K.-I. Kobayashi, T. Kimura, H. Sawada, K. Terakura, Y. Tokura, *Nature* **1998**, *395*, 677.
- [4] T. H. Kim, M. Uehara, S.-W. Cheong, S. Lee, *Appl. Phys. Lett.* **1999**, *74*, 1737.
- [5] M. García-Hernández, J. L. Martínez, M. J. Martínez-Lope, M. T. Casais, J. A. Alonso, *Phys. Rev. Lett.* **2001**, *86*, 2443.
- [6] L. Balcells, J. Navarro, M. Bibes, A. Roig, B. Martínez, J. Fontcuberta, *Appl. Phys. Lett.* **2001**, *78*, 781.
- [7] D. Sánchez, J. A. Alonso, M. García-Hernández, M. J. Martínez-Lope, M. T. Casais, J. L. Martínez, *J. Mater. Chem.* **2003**, *13*, 1771–1777.
- [8] H. M. Yang, W. Y. Lee, H. Han, B. W. Lee, C. S. Kim, *J. Appl. Phys.* **2003**, *93*, 6987–6989.
- [9] M. Retuerto, M. J. Martínez-Lope, M. García-Hernández, J. A. Alonso, *Eur. J. Inorg. Chem.* **2009**, *8*, 1103–1109.
- [10] K.-I. Kobayashi, T. Okuda, Y. Tomioka, T. Kimura, Y. Tokura, *J. Magn. Magn. Mater.* **2000**, *218*, 17.
- [11] S. Ray, A. Kumar, S. Majumdar, E. V. Sampathkumaran, D. D. Sarma, *J. Phys. Condens. Matter* **2001**, *13*, 607.
- [12] H. Chang, M. García-Hernández, M. Retuerto, J. A. Alonso, *Phys. Rev. B* **2006**, *73*, 1044171–6.
- [13] J. B. Shi, P. H. Peng, Y. Y. Fan, C. Y. Lee, W. T. Lai, H. C. Ku, H. Z. Chen, S. L. Young, *Phys. B* **2003**, *329–333*, 731–732.
- [14] T.-T. Fang, T.-F. Ko, *J. Am. Ceram. Soc.* **2003**, *86*, 1453–1455.
- [15] G. Y. Liu, G. H. Rao, X. M. Feng, H. F. Yang, Z. W. Ouyang, W. F. Liu, J. K. Liang, *J. Alloys Compd.* **2003**, *353*, 42–47.
- [16] Y. Markandeya, K. Suresh, G. Bhikshamaiah, *J. Alloys Compd.* **2011**, *509*, 9598–9603.
- [17] M. C. Viola, J. A. Alonso, J. C. Pedregosa, R. E. Carbonio, *Eur. J. Inorg. Chem.* **2005**, 1559–1564.
- [18] C. A. López, M. C. Viola, J. C. Pedregosa, J. A. Alonso, M. T. Fernández-Díaz, *Eur. J. Inorg. Chem.* **2010**, *26*, 4110–4120.
- [19] C. A. López, M. C. Viola, J. C. Pedregosa, R. C. Mercader, *Mater. Res. Bull.* **2010**, *45*, 1520–1526.
- [20] V. Nassif, R. E. Carbonio, J. A. Alonso, *J. Solid State Chem.* **1999**, *146*, 266–270.
- [21] E. A. Owen, G. I. Williams, *J. Sci. Instrum.* **1954**, *31*, 49.
- [22] D. Niebieskikwiat, R. D. Sánchez, A. Caneiro, L. Morales, M. Vásquez-Mansilla, F. Rivadulla, L. E. Hueso, *Phys. Rev. B* **2000**, *62*, 3340–3345.
- [23] M. Tovar, M. T. Causa, A. Butera, J. Navarro, B. Martínez, J. Fontcuberta, M. C. G. Passeggi, *Phys. Rev. B* **2002**, *66*, 0244091–5.
- [24] K. D. Bowers, J. Owen, *Rep. Prog. Phys.* **1955**, *18*, 304–373.
- [25] T. F. Rosenbaum, S. A. Carter, *J. Solid State Chem.* **1990**, *88*, 94–103.
- [26] B. Chattopadhyay, A. Poddar, S. Das, R. Majumder, R. Ranjanathan, *J. Alloys Compd.* **2004**, *366*, 28–33.
- [27] E. K. Hemery, G. V. M. Williams, H. J. Trodahl, *Phys. Rev. B* **2006**, *74*, 0544231–5.
- [28] E. K. Hemery, G. V. M. Williamsa, H. J. Trodahl, *J. Magn. Magn. Mater.* **2007**, *310*, 1958–1960.
- [29] H. J. Trodahl, *Phys. Rev. B* **1995**, *51*, 6175–6178.
- [30] N. Kaurav, K. K. Choudhary, D. Varshney, *J. Phys. Conf. Ser.* **2007**, *92*, 0121281–4.
- [31] N. F. Mott, H. Jones, *The Theory of the Properties of Metals and Alloys*, Dove Publications, New York, **1958**, p. 310.
- [32] Y. Yasukawa, J. Lindén, T. S. Chan, R. S. Liu, H. Yamauchi, M. Karppinen, *J. Solid State Chem.* **2004**, *177*, 2655–2662.
- [33] A. Maignan, B. Raveau, C. Martin, M. Hervieu, *J. Solid State Chem.* **1999**, *144*, 224–227.
- [34] H. M. Rietveld, *J. Appl. Crystallogr.* **1969**, *2*, 65–71.
- [35] J. Rodríguez-Carvajal, *Phys. B* **1993**, *192*, 55–69.

Received: March 31, 2014

Published Online: June 27, 2014